crystals

MDPI

Article

Mechanical, Tribological, and Corrosion Resistance Properties of $(TiAl_xCrNbY)N_y$ High-Entropy Coatings Synthesized Through Hybrid Reactive Magnetron Sputtering

Nicolae C. Zoita *, Mihaela Dinu, Anca C. Parau, Iulian Pana and Adrian E. Kiss

National Institute of Research and Development for Optoelectronics—INOE 2000, 409 Atomiștilor Street, 077125 Magurele, Romania

* Correspondence: cnzoita@inoe.ro

Abstract: This study investigates the effects of aluminum and nitrogen content on the microstructure, mechanical properties, and tribological performance of high-entropy coatings based on $(TiCrAl_xNbY)N_y$ systems. Using a hybrid magnetron sputtering technique, both metallic and nitride coatings were synthesized and evaluated. Increasing the aluminum concentration led to a transition from a crystalline to a nanocrystalline and nearly amorphous (NC/A) structure, with the $TiAl_{0.5}CrNbY$ sample (11.8% Al) exhibiting the best balance of hardness (6.8 GPa), elastic modulus (87.1 GPa), and coefficient of friction (0.64). The addition of nitrogen further enhanced these properties, transitioning the coatings to a denser fine-grained FCC structure. The HN2 sample (45.8% nitrogen) displayed the highest hardness (21.8 GPa) but increased brittleness, while the HN1 sample (32.9% nitrogen) provided an optimal balance of hardness (14.3 GPa), elastic modulus (127.5 GPa), coefficient of friction (0.60), and wear resistance (21.2×10^{-6} mm^3/Nm). Electrochemical impedance spectroscopy revealed improved corrosion resistance for the HN1 sample due to its dense microstructure. Overall, the $(TiAl_{0.5}CrNbY)N_{0.5}$ coating achieved the best performance for friction applications, such as break and clutch systems, requiring high coefficients of friction, high wear resistance, and durability.

Keywords: high-entropy alloys; microstructure; mechanical properties; tribological properties; electrochemical properties

Citation: Zoita, N.C.; Dinu, M.; Parau, A.C.; Pana, I.; Kiss, A.E. Mechanical, Tribological, and Corrosion Resistance Properties of $(TiAl_xCrNbY)N_y$ High-Entropy Coatings Synthesized Through Hybrid Reactive Magnetron Sputtering. *Crystals* **2024**, *14*, 993. https://doi.org/10.3390/cryst14110993

Academic Editor: Mingyi Zheng

Received: 24 October 2024
Revised: 11 November 2024
Accepted: 14 November 2024
Published: 17 November 2024

1. Introduction

Certain industries, such as the automotive industry, machine tools, and structural components require materials that offer exceptional mechanical properties, along with high wear resistance, thermal stability, and corrosion resistance. These features are critical for preventing tribological damage when operating in critical conditions, such as high speeds and elevated temperatures. An effective approach to achieving these desired properties is by coating components with specialized alloys. The current trend emphasizes the development of multi-principal element alloys, known as high-entropy alloys (HEAs) [1,2]. Composed of at least five principal metallic elements in near-equal atomic ratios, these alloys exhibit superior mechanical, tribological, thermal, and corrosion resistance properties compared to traditional alloys [1,3,4]. These enhanced properties are attributed to four postulated mechanisms, known as the "core effects" [5]:

The high configurational entropy effect, which increases the mutual solubility of the constituent elements in HEAs, promotes the formation of thermodynamically stable, simple solid solution phases with random site occupancy, such as face-centered cubic (FCC), body-centered cubic (BCC), and hexagonal close-packed (HCP) phases [6–8].

The sluggish diffusion effect in HEAs refers to the reduced atomic mobility within these alloys. This occurs because in the solid solution phases of HEAs, each lattice site is surrounded by a more diverse array of atoms than in conventional alloys [9]. This results

in slower diffusion rates, enhancing thermal structural stability [10–12] and facilitating the formation of nanostructured or amorphous phases [13–15];

The severe lattice distortion effect in HEAs results from substantial atomic size mismatches, leading to atomic-level strains. This effect influences various properties, including enhanced mechanical strength through solid solution strengthening [16,17], as well as decreased electrical and thermal conductivity [18,19]. In cases of extreme distortion, it can even lead to the formation of nanostructured or amorphous phases [2,20,21].

The cocktail effect describes the cumulative impact of combining multiple principal elements [9], with each element contributing to the alloy's physical and chemical properties. This effect might impact various characteristics, such as mechanical strength [22], corrosion resistance [23,24], wear resistance [23,24], catalytic efficiency [25,26], and magnetic properties [27,28], among others.

However, recent studies indicate that configurational entropy may not be the dominant factor in the formation of single-phase solid solution microstructures with simple crystal structures in HEAs. Instead, phase stability in HEAs appears to be influenced by a combination of thermophysical factors, such as the mixing enthalpy, atomic size mismatch, valence electron concentration, and electronegativity [29–32]. Many HEA systems undergo phase separation, resulting in the coexistence of two or more simple HEA phases, as well as intermetallic phases referred to as high-entropy intermetallic phases (HEIs) [33–35]. Dual- and multi-phase HEAs behave similarly to traditional composites or nanocomposites, offering enhanced or customizable properties depending on the volume fraction of each phase [20,36]. Over the past decade, there has been a growing focus on studying and developing multi-phase HEAs [37–41], which are now considered one of the key strategies for the development of new materials [34].

The high-entropy concept has also been extended to ceramic materials. To date, several types of high-entropy ceramics have been developed, including high-entropy borides (HEBs) [42,43], carbides (HECs) [44–46], nitrides (HENs) [47,48], oxides (HEOs) [49,50], and silicides (HESs) [51,52], by incorporating B, C, N, O, or Si, respectively, into the metallic matrix. These materials show high potential for both structural and functional applications [53]. Specifically, HEN coatings have been investigated for their potential as high-temperature protective coatings due to their oxidation and corrosion resistance, which can be attributed to sluggish diffusion kinetics and the cocktail effect when specific elements, such as Al, Cr, or Si, are included [54–56]. HENs have also demonstrated high to ultra-high hardness, reaching up to 60 GPa [57], along with good wear resistance [58] and thermal stability. Notable examples include (TiZrHfVTa), which exhibited a single-phase FCC structure with uniform elemental distribution up to an annealing temperature of 1350 °C [59], (TiVZrNbHf)N, which maintained stability up to 1100 °C [57], and (AlCrTaTiZr)N, which remained stable without phase separation under thermal annealing at 1000 °C for 120 min [60].

In one review paper [55], it is emphasized that the structure and properties of HEN coatings are notably influenced by the choice of constituent elements, along with the deposition method and the specific processing parameters.

For friction applications that require a medium-high friction coefficient and wear-resistant surfaces, this work synthesizes and investigates the properties of a $(TiCrAl_xNbY)N_y$ metallic and ceramic coating. The constituent elements are known for their high strength and wear resistance, making them desirable for tribological use. Cr, Nb, and Ti are recognized for their ability to form highly wear-resistant alloys [55,61,62], while Al, Nb, Cr, and Y are often employed to enhance strength, corrosion resistance, and thermal stability [63,64]. In non-stoichiometric HEAs, previous studies have shown that aluminum content plays a significant role in influencing the microstructure and mechanical performance [65]. Additionally, in the presence of nitrogen, all proposed elements form strong bonds with nitrogen, especially the early transition metals. The lowest formation enthalpy corresponds to the Cr-N bond, $\Delta Hf = -117.15$ kJ/mol, while the highest corresponds to the Ti-N bond, $\Delta Hf = -338$ kJ/mol [66].

To our knowledge, the $(TiAl_xCrNbY)N_\gamma$ high-entropy system was never investigated. This study uniquely explores the combined effects of aluminum and nitrogen variations on the microstructure and performance of $(TiAl_xCrNbY)N_\gamma$ coatings, providing new insights into optimizing high-entropy nitride coatings for enhanced mechanical, tribological, and corrosion-resistant properties through a hybrid reactive HiPIMS/DCMS magnetron sputtering approach. This study first examines the effect of the Al concentration on the metallic system. Once the optimal composition for tribological performance is identified, nitrogen is added to further improve the tribological and mechanical properties.

2. Materials and Methods

Metallic $TiAl_xCrNbY$ and nitride multi-principal alloy coatings $(TiAl_{0.5}CrNbY)N_x$ were deposited on C45 steel (refer to Table 1) and Si (100) substrates using a hybrid magnetron sputtering process that integrates direct current magnetron sputtering (DCMS) with high-power impulse magnetron sputtering (HiPIMS). This hybrid HiPIMS/DCMS configuration was chosen to enhance adhesion, increase film density, and improve the microstructural control. These enhancements are attributed to the high density of ionized particles generated by the high-power pulsed discharge, which actively bombard the film's growing surface during deposition [45,67,68]. The deposition setup (AJA-ATC-ORION by AJA International Inc., Hingham, MA, USA) utilized five unbalanced magnetrons compatible with 50.8 mm targets. HiPIMS powered the Al and Cr targets, while DCMS powered the Ti, Nb, and Y targets. An additional RF source provided bias to the substrate. Except for the HiPIMS power supply, which was laboratory-built with a 1.5 Ω output impedance and a maximum output of 1000 V/150 A, all power supplies were from AJA International Inc. All targets, with 99.99% purity, were provided by Kurt J. Lesker Company, Jefferson Hills, PA, USA.

Table 1. Elemental composition of C45 steel substrate.

Elements	C	Mn	Cr	Si	Ni	Mo	Fe
C45 (wt. %)	0.436	0.639	0.351	0.291	0.294	0.089	balance

Prior to deposition, substrates underwent ultrasonic cleaning in isopropyl alcohol for 15 min. They were subsequently degassed in the deposition chamber at 300 °C for 30 min, followed by a 10 min sputter-etching process using a 50 W RF argon plasma (0.67 Pa gas pressure). Before each deposition, the chamber was evacuated to approximately 1×10^{-5} Pa. Films were then deposited in either an Ar or Ar + N_2 reactive atmosphere, with nitrogen levels adjusted based on the target properties (HEA or HEN coatings). To obtain HEA coatings with varying Al concentrations, the frequency of HiPIMS impulses applied to the Al cathode was adjusted. Similarly, to produce HENs with different nitrogen concentrations, the flow rate of N_2 gas was regulated. Ar and N_2 gases have a purity grade of 6.0 (Linde Gaz Romania, Bucharest, Romania).

If not specified otherwise, experiments were performed on films deposited on C45 steel substrates. The elemental composition of the coatings was analyzed using energy-dispersive X-ray spectroscopy (EDS) on a TM3030 Plus (Hitachi High-Technologies Corporation, Tokyo, Japan) scanning electron microscope (SEM) fitted with a Bruker Quantax70 EDS system. EDS spectra were calibrated using the Cu-Kα (8.037 keV) and Cu-Lα (0.926 keV) emission lines from a standard copper sample. All spectra were recorded over the 0–15 keV energy range for 1200 s. To avoid interference from chromium in C45 substrates, elemental analysis was performed on films deposited on Si substrates.

The crystallographic structure of the coatings was investigated through X-ray diffraction (XRD) using a SmartLab diffractometer (Rigaku, Tokyo, Japan) equipped with a 9 kW Cu rotating anode and a 5-axis vertical goniometer with a 0.3 m radius. Operating in parallel beam mode, the diffractometer included high-resolution optics, such as a 2-bounce Ge (220) monochromator in the incident beam path to isolate Cu-Kα1 radiation (λ = 1.5406 Å).

Horizontal and vertical incident slits were set at 1.0 mm and 5.0 mm, respectively. XRD patterns were collected over a 2θ range of 20° to 100°, with a resolution of 0.005° and an acquisition rate of 1.0°/min. Data analysis was conducted with Powder X-ray Diffraction Profile (PDXL v. 2.9, Rigaku) software utilizing the ICDD PDF-4 + XRD database.

The average film mass density was measured using X-ray reflectivity (XRR) on the mentioned abovediffractometer. XRR patterns were captured with horizontal and vertical slits set at 0.15 mm and 5.0 mm, respectively. Measurements spanned a 2θ range from 0.1° to 3.0°, with a resolution of 0.001° and an acquisition speed of 0.16°/min. The Rigaku GlobalFit v. 2.0 software package was used to analyze XRR patterns by applying a two-layer model: a thin top layer representing the air-contaminated surface and a second layer representing the coating's actual properties. Due to the coating thickness exceeding the X-ray penetration depth (<500 nm), the coating–substrate interface was inaccessible, and the second layer was treated as bulk material.

Surface morphology was studied using atomic force microscopy (AFM) on a Veeco Innova AFM system placed on a vibration-damped table. Images were recorded over a 3 μm × 3 μm area with a resolution of 1024 × 1024 pixels and a scan rate of 0.7 Hz. The setup used commercial pyramidal *p*-doped silicon tips (model RTESPA), attached to a 125 μm cantilever with a resonance frequency of about 332 kHz and a nominal force constant of approximately 40 N/m. Topographical image analysis was performed with Gwyddion software, version 2.30 [69].

Nanoindentation testing was conducted with a Hysitron TI Premier unit equipped with a Berkovich tip (100 nm radius of curvature, included angle of 142.3°). Before testing, certain factors, such as thermal drift, initial penetration depth, machine compliance, and indenter area function, were accounted for to improve the accuracy [63]. Force calibration was carried out on a standard fused quartz sample with hardness (H) and elastic modulus (E) values of 9.25 GPa ± 10% and 69.6 GPa ± 10%, respectively. Following ISO 14577-1:2015 standards [70], maximum indentation and contact depths were maintained between 40 nm and 1/10 of the coating's thickness to limit the substrate's influence and to accommodate the Berkovich tip's geometry. For each sample, a maximum indentation load of 5 mN was applied, with loading and unloading times of 7 s and a 2 s hold time at the peak load. Indentation points were spaced 5 μm apart to avoid interference.

Tribology tests were conducted using a laboratory-built pin-on-disc tribometer compliant with ASTM G99-23 (https://www.astm.org/standards/g99 (accessed on 16 October 2024)). The tribometer is configured with a stationary pin supported by a lever arm, allowing the pin to be pressed against the horizontally mounted rotating disc sample under a controlled normal load. The normal load is applied using standardized weights. The friction force is calibrated periodically (i.e., the relationship between a transverse load applied to the lever arm and the response of the strain gauge bridge). Additionally, the coefficient of friction (COF) and wear rate of a test disc sample made from 100Cr6 steel (equivalent to AISI 52,100 steel) were measured to verify the functionality and accuracy of the system. All tribological tests were performed at a room temperature and relative humidity of 23 °C and 40%, respectively. Both the ball (a synthetic sapphire ball with a 6 mm diameter) and the sample were cleaned with isopropyl alcohol prior to each test. Each test was conducted with a 1 N normal load and a 10 cm/s sliding speed along an 8 mm radius circular track. To limit the substrate's influence, the sliding distance, D, was set to 50 m for HEA coatings and 100 m for HEN coatings. The reported mechanical and tribological properties of the coatings are based on the average values obtained from a minimum of three measurements conducted on three separate samples produced within the same batch. Wear track profiles were measured using a Bruker Dektak 150 surface profilometer on at least 8 positions of each wear track, from which the mean wear track volume, V, was calculated. The wear rate, K, was calculated using the $K = V/(F \cdot D)$ equation.

To assess the worn surfaces after tribological measurements, the elemental composition and surface morphology of the selected areas were analyzed using SEM and EDS techniques. For observations of growth patterns and the microstructure, high-resolution cross-sectional

SEM (HR-SEM) micrographs were captured using a NanoSAM LAB S (Scienta Omicron, Uppsala, Sweden).

Electrochemical impedance spectroscopy (EIS) was performed to evaluate the electrochemical behavior of coatings. Samples were immersed in a 0.06 M NaCl solution for 12 h at room temperature. EIS data were collected across a frequency range of 0.2 to 10^3 Hz using a 10 mV amplitude sinusoidal excitation signal. A VersaSTAT 3 potentiostat/galvanostat system (Princeton Applied Research, Oak Ridge, TN. USA) with a standard three-electrode cell setup was used for the measurements. It consists of a Ag/AgCl reference electrode (0.197 V vs. SHE), a platinum counter electrode, and the tested sample as the working electrode. Data were recorded using VersaStudio software (version 2.60.6) and analyzed with ZView software (Scribner Associates Inc., Southern Pines, NC, USA), version 12136-4.

3. Results and Discussions

3.1. Influence of Al Concentration

3.1.1. Microstructural Characteristics of $TiAl_xCrNbY$/C45 ($0.12 \leq x \leq 1$) Coatings

The elemental composition of $TiAl_xCrNbY$ coatings, determined through EDS analysis, is presented in Table 2 in terms of atomic concentrations along with the approximate stoichiometry formulas. It is noted that aside from aluminum, whose concentration varied from approximately 3.0 at.% (sample H1) to around 20 at.% (sample H4), all other elements maintained a near-equiatomic ratio.

Table 2. Elemental composition of the coatings and the valence electron concentration (VEC).

Sample	Ti (at. %)	Cr (at. %)	Nb (at. %)	Y (at. %)	Al (at. %)	VEC	Stoichiometry
H1	24.3	23.4	25.1	24.2	3.0	4.45	$TiAl_{0.12}CrNbY$
H2	23.2	22.8	23.7	24.1	6.2	4.37	$TiAl_{0.25}CrNbY$
H3	22.3	20.6	22.3	23.0	11.8	4.28	$TiAl_{0.5}CrNbY$
H4	20.1	19.9	19.8	20.4	19.8	4.19	TiAlCrNbY

The out-of-plane XRD patterns corresponding to samples H1–H4 are shown in Figure 1. In addition to substrate features labeled with "S", the XRD pattern of sample H1 displays several peaks at approximately 30.35°, 39.17°, and 63.71°. The noticeable differences in the widths of the first two features suggest the presence of multiple crystallographic phases. Specifically, the peak at 30.35° has a full width at half maximum (FWHM) of about 1.1°, while the feature at 39.17° has an FWHM of approximately 4.9°, which is more than four times broader. This observation implies a dual-phase crystallographic structure: a crystalline phase represented by the narrow peaks and a nanocrystalline approaching amorphous (NC/A) phase indicated by the broad peak. The mean crystallite size, calculated using the Scherrer equation [71], is approximately 7.8 nm for the crystalline phase and 1.9 nm for the nanocrystalline phase, this latter value being characteristic of NC/A structures. Moreover, the feature attributed to the NC/A phase exhibits a purely Gaussian shape, with no visible shoulder that would suggest a superposition of multiple peaks. Therefore, attributing this peak to an NC/A phase should be accurate.

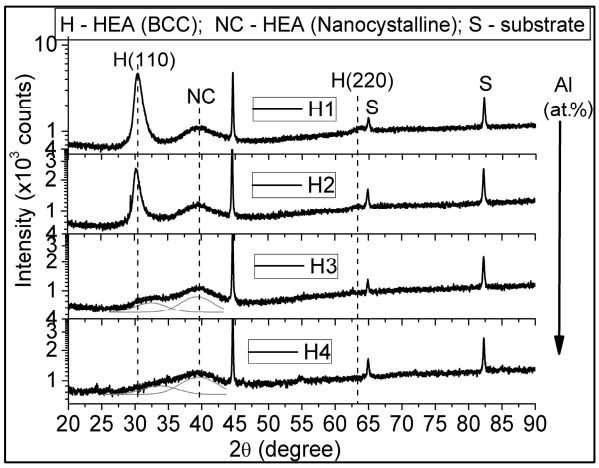

Figure 1. 2θ/θ X-ray diffraction patterns corresponding to H1–H4 coatings.

The valence electron concentration (VEC) rule [32,71,72] is an empirically derived criterion used to predict the structural phases of high-entropy alloys and serves as a useful indicator of phase stability. According to this rule, an HEA is likely to form an FCC solid solution phase when VEC $\geq$ 8.0, a BCC phase when VEC < 6.87, and an FCC+BCC mixture if VEC falls between these values. The VEC of an alloy is calculated as the weighted average of the valence electron concentrations of its constituent elements [72,73]. $VEC = \sum_i (c_i (VEC)_i)$, where c_i and $(VEC)_i$ represent the atomic percentage and the VEC for the ith element, respectively. Using the $(VEC)_i$ values provided in reference [74], the calculated VEC for sample H1 is approximately 4.45 (Table 2), which is well below 6.87. This indicates that sample H1 is likely to include a BCC structure. Accordingly, we assigned the sharp diffraction peaks observed around 30.35° and 63.71° to the (110) and (220) reflections, respectively, corresponding to a simple BCC (Im–3 m) solid solution phase, with an estimated lattice parameter of a = 3.469 Å, labeled as "H" in Figure 1. This finding aligns with other high-entropy systems [75,76], suggesting the formation of a simple crystallographic phase instead of complex intermetallic phases, confirming the synthesis of a high-entropy material.

With an increase in the Al content to 6.2% (sample H2), the XRD peaks seen in the XRD pattern corresponding to sample H1 are preserved, presenting comparable widths, but the (110) peak shifts to a slightly higher 2θ value by approximately 0.12°, indicating a lattice parameter reduction of about 0.017 Å. The intensity of the (110) reflection also decreases, suggesting a reduction in the crystalline BCC phase fraction. This effect becomes more pronounced for samples H3 and H4, with much higher Al contents of about 11.8 at.% and 19.8 at.%, respectively. The (110) BCC peak is still present but significantly broadened, weakened, and shifted further to higher 2θ values. Deconvolution of the broad feature observed in the 30–40° range of the XRD patterns corresponding to the H3 and H4 patterns reveals two broad, Gaussian-shaped components (Figure 1) corresponding to two nanostructured phases: BCC and FCC nanostructured solid solutions. The attribution to an FCC structure of the broad feature observed at about 39.2° in all H1–H4 samples is in agreement with previous reports on the near-stoichiometric TiAlCrNbY system [77].

The shift of the (110) BCC peak to higher 2θ values with increasing Al content is explained by the lattice cell decrease as more aluminium atoms (of low atomic radius, 1.432 Å) and, consequently, less Yttrium atoms (of high atomic radius, 1.802 Å) enter the unit cell. We mention that Y atoms are the largest atoms in this system. The mean atomic radius, defined as $\bar{r} = \sum_i (c_i r_i)$, where r_i is the atomic radius of the ith element, decreases from about $\bar{r}$ = 1.487 Å (sample H1) to about $\bar{r}$ = 1.475 Å (sample H4).

It should be noted that a large atomic size difference between the atomic components of a multicomponent system favors BCC over FCC [78]. This can be attributed to the fact that the BCC structure has fewer constraints compared to the FCC structure,

allowing it to accommodate atoms of varying sizes with the cost of a lower strain energy [78]. Moreover, a much larger size discrepancy violates the Hume–Rothery (H-R) rules for binary solid solution formation, thereby destabilizing a crystalline solid solution and enhancing the glass-forming ability [79]. Based on the H-R rules, general formation criteria for ideal multicomponent solid solutions have been suggested. Such formation rules are the subject of ongoing discussion, with examples presented that both support and contradict these rules [80,81]. Most prominent are the topologic and thermodynamic criteria that approximate the limits of the atomic size difference (δ) and of the enthalpy of mixing (ΔH_{MCA}^{mix}): δ < 7% and −12 kJ/mol < ΔH_{MCA}^{mix} < 5 kJ/mol) [7,78,82]. Here, the atomic size difference is defined by $\delta = \sqrt{\sum_i ci\left(1-\frac{r_i}{\bar{r}}\right)^2}$ and the mixing enthalpy of a multicomponent system, if only binary chemical interactions are considered, by $\Delta H_{MCA}^{mix} = \sum_{i,j} c_i c_j \left(4\Delta H_{i-j}^{mix}\right)$, where ΔH_{i-j}^{mix} is the mixing enthalpy of binary solid solutions [31].

For Samples H1–H4, δ varies from 13.3% to about 12.20%, values much larger than ~7%. It seems that the development of the NC/A phase could be due to the relatively large value of the atomic size difference. The amorphization is accentuated by increasing the content of Al due to the large negative mixing enthalpy of Al with the other elements. The mixing enthalpy of the binary solid solutions Al-Ti, Al-Y, Al-Cr, and Al-Nb comprises highly negative values: ΔH_{Al-Ti}^{mix} = −30 kJ/mol, ΔH_{Al-Y}^{mix} = −38 kJ/mol, ΔH_{Al-Cr}^{mix} = −30 kJ/mol, and ΔH_{Al-Nb}^{mix} = −18 kJ/mol, respectively [83]. ΔH_{MCA}^{mix} increases on a negative scale from about −4.0 kJ/mol when the Al content is 0% to about −17.9 kJ/mol when the Al concentration is about 20% (H4 sample).

The nano- and micro-structural investigation performed through AFM and cross-sectional SEM confirm the XRD findings. Figure 2a,b present AFM images of the coating surfaces covering a 3 μm × 3 μm surface area corresponding to the H1 and H4 samples. The surface morphology is dominated by fine domed columnar grains. The size of the grains decreases with increasing aluminum content of the coatings such that the surface morphology transforms to a glassy morphology characteristic of NC/A materials when the Al content is about 20 at.% (sample H4), in agreement with XRD findings. In consequence, the root mean square (RMS) surface roughness gradually decreases from about 0.95 nm (sample H1) to about 0.35 nm (sample H4).

Cross-sectional HR-SEM investigations confirm a crystalline columnar growth of sample H1, as shown in Figure 2c, with a tendency towards column coalescence when the coating thickness exceeds approximately 2 μm. In contrast, sample H4 shows a dense, ultrafine-grained, nearly featureless (glassy) structure. For sample H1, the columns are believed to consist of BCC crystallites, while the NC/A material indicated by XRD investigations is thought to be deposited in the intercolumnar and intergranular spaces. As the Al content increases, the microstructure transitions to a dense, fine, nano-granular structure consisting of both BCC and FCC phases, which are homogeneously distributed. This is consistent with observations reported by other authors using HR-SEM and transmission electron microscopy (TEM) [84]. In both cases, samples H1 and H4, we could not detect through HR-SEM/EDS any compositional separations but only a homogeneous distribution of elements on the cross-section of the coatings. Figure 3 presents the cross-sectional mappings of elements corresponding to sample H1 over an area of 2.15 × 1.54 μm^2, centered in Figure 2c, demonstrating a homogeneous distribution of elements. Further TEM and selected area electron diffraction (SAED) investigations are planned to clarify the structure of the second phase, which is thought to be FCC here.

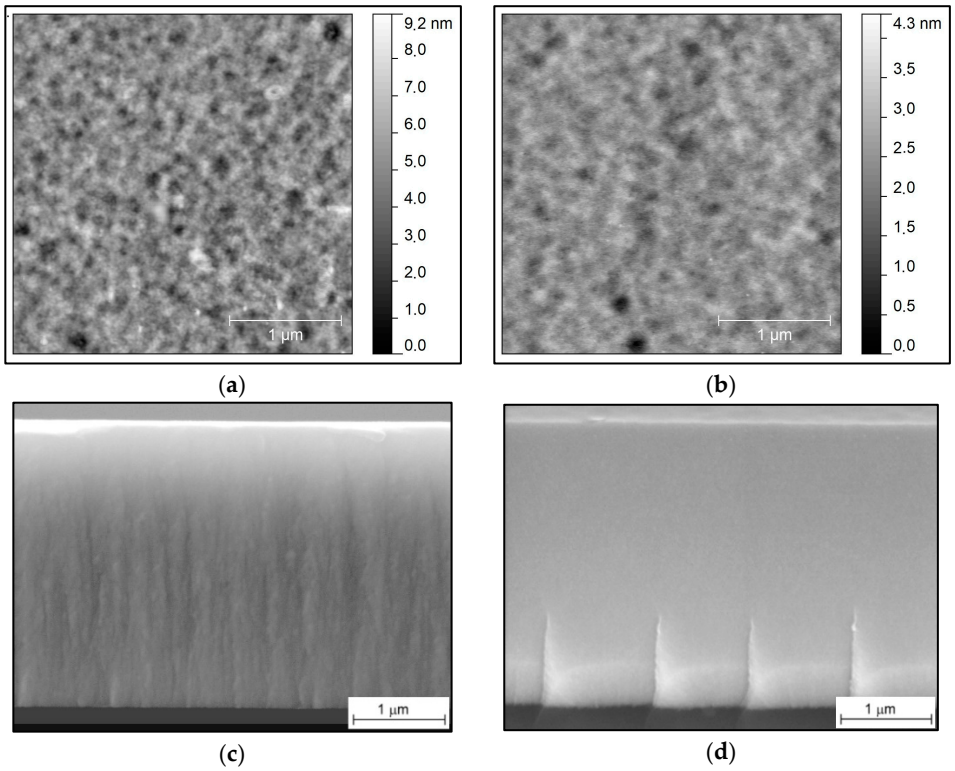

Figure 2. AFM surface images (3 × 3 µm^2) corresponding to (**a**) H1 and (**b**) H4 samples. Cross-sectional HR-SEM images corresponding to (**c**) H1 and (**d**) H4 samples.

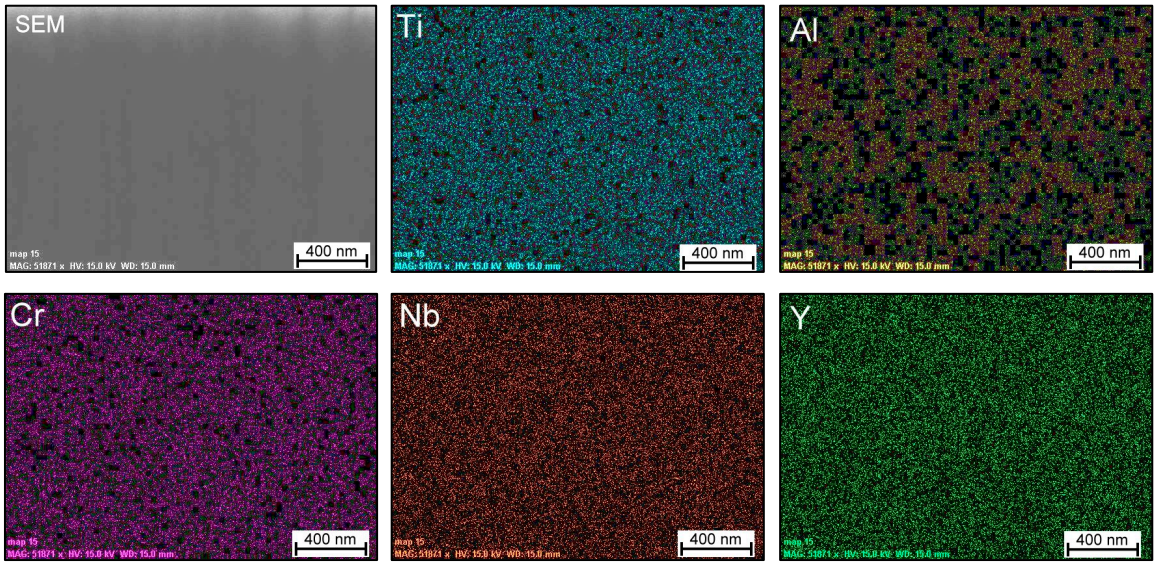

Figure 3. Elemental cross-sectional mapping corresponding to H1 coating, 2.15 × 1.54 µm^2.

3.1.2. Mechanical and Tribological Properties of $TiAl_xCrNbY$ ($0.12 \leq x \leq 1$)

The mechanical characteristics—hardness (H) and Young's modulus (E)—of $TiAl_xCrNbY$ HEA coatings (samples H1–4) were investigated using a nanoindentation technique. Figure 4a,b present the dependence of the H and E, respectively, on the Al concentration of the coatings. The samples exhibit moderate hardness in the range of 6–7 GPa and relatively low elastic modulus values in the range of 70–80 GPa. The sample H1 presents the lowest H and E values of about 6.1 GPa and 81 GPa, respectively. As the Al concentration increases, both mechanical properties improve until the Al content reaches around 12.5% (sample H3), where H reaches 6.8 GPa and E reaches 87.1 GPa. A slight decline follows

as the Al concentration increases to about 20% (sample H4), with H decreasing to 6.7 GPa and E to 86.2 GPa. Based on microstructural analysis, it appears that the mechanical characteristics are predominantly influenced by the microstructure, which is in line with the Hall–Petch relationship, which describes an inverse proportionality between hardness and grain size [85]. The XRD, AFM, and cross-SEM investigations demonstrated an accentuate crystallite size decrease when the Al content is increased from about 6.8 at.% (sample H2) to about 11.8 at.% (sample H3), and only a slight further decrease when the Al content is raised to about 20 at.%. It is known that the Hall–Petch effect is valuable for grain sizes larger than a critical value. Reverse Hall–Petch behavior occurs when grain sizes fall below this critical threshold [86]. It could be the case that the mean grain size corresponding to sample H3 is approaching the critical value.

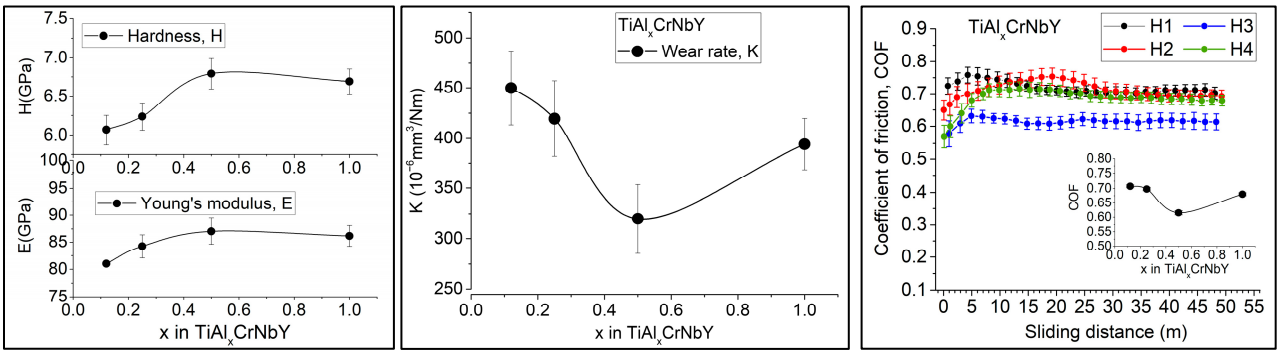

(**a**) (**b**) (**c**)

Figure 4. (**a**) The averaged values of hardness (H) and Young's modulus (E). (**b**) Wear rate. (**c**) Friction coefficient evolution.

The tribological properties, i.e., the wear rate, follow the Archard dependence on hardness [87]. Sample H3 exhibits the lowest wear rate, with a value of 315 × 10^{-6} mm^3/Nm (Figure 4b), which is a lower value by about 30% compared to sample H1. The coefficient of friction (COF) shows less variation with changes in the Al content. COF reaches steady values in the range of 0.64–0.68 on the last 20–30 m of the sliding testing distance (Figure 4c and inset). Each point in Figure 4c represents the average coefficient of friction recorded over approximately 2 m of sliding distance and subsequently averaged across the values obtained for each of the three specimens for each stoichiometry. The error bars represent the standard deviation of these averages, calculated using the principles of error propagation.

For friction applications, the $TiAl_{0.5}CrNbY$ coatings (sample H3) demonstrate the best combination of mechanical and tribological characteristics. To further improve the tribological properties, especially the wear rate, while maintaining a high COF, Nitrogen was incorporated into the composition of $TiAl_{0.5}CrNbY$ (sample H3). Two sets of samples with varying nitrogen content were produced, and the effect of nitrogen addition on the $TiAl_{0.5}CrNbY$ coatings will be discussed in the following section.

3.2. Influence of Nitrogen Concentration

3.2.1. Microstructural Characteristics of $(TiAl_{0.5}CrNbY)N_x$/C45 ($0 \leq x \leq 0.85$) Coatings

Table 3 presents the elemental compositions of the HEN coatings. Two samples were prepared with nitrogen concentrations of about 32.9 at.% and 45.8 at.%, with approximate stoichiometries of $(TiAl_{0.5}CrNbY)N_{0.5}$ and $(TiAl_{0.5}CrNbY)N_{0.85}$, respectively.

Table 3. Elemental compositions of $(TiAl_{0.5}CrNbY)$ N_x coatings (at. %).

Sample	Ti	Cr	Al	Nb	Y	N	Stoichiometry
HN1	14.2	15.0	8.2	14.9	14.6	32.9	$(TiAl_{0.5}CrNbY)N_{0.5}$
HN2	11.8	12.4	6.7	11.9	11.4	45.8	$(TiAl_{0.5}CrNbY)N_{0.85}$

The XRD patterns corresponding to H3-$TiAl_{0.5}CrNbY$, HN1, and HN2 coatings are presented in Figure 5a. The diffraction pattern corresponding to the HN1 sample, containing 32.9 at. % of nitrogen, shows only a broad feature centered at about 2θ = 39.0°. The BCC (110) observed in the XRD pattern of H3 sample completely vanished. Upon further increasing the nitrogen content to 45.8% (HN2 sample), the NC/A feature disappears, and weak diffraction lines are identified at about 35.13°, 40.72°, 59.38° and 71.02°. These diffraction lines can be attributed to (111), (200), (220), and (311) planes of an FCC solid solution with lattice parameter of a = 4.377 Å, which is similar to ICDD reference 04-019-7798. The mean crystallite size and lattice strain, calculated using the Halder–Wagner method [88] are 35.0 ± 1.3 Å and 0.01%, respectively, with the latter suggesting that the material is completely relaxed.

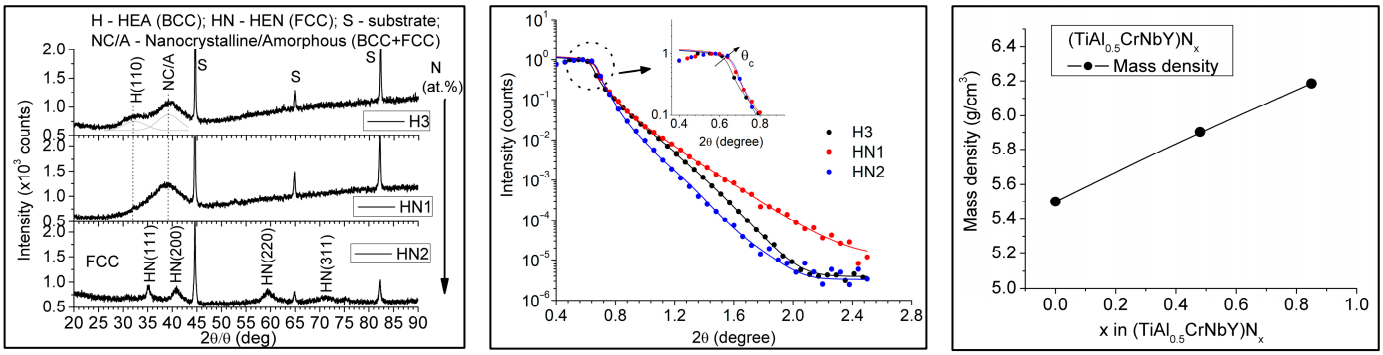

(**a**) (**b**) (**c**)

Figure 5. (**a**) 2θ/θ X-ray diffraction patterns and (**b**) XRR experimental (scattered points) and simulated patterns (continuous lines) corresponding to samples H3, HN1, and HN2; (**c**) average mass density variation with nitrogen content.

It should be noted that all metal elements (Ti, Cr, Al, Nb, Y) can form FCC-structured nitrides. Consequently, in the presence of nitrogen atoms, the metal atoms preferentially form bonds with nitrogen atoms, as the bond energy between metal and nitrogen atoms (Me-N) is much greater than the bond energy between metal atoms (Me-Me) [89,90]. Moreover, the lattice parameters of transition metal nitrides have comparable values. As a result, the addition of nitrogen and subsequently increasing the nitrogen content in the coatings promotes the formation of FCC nitrides, thus promoting long-distance lattice ordering and effectively improving the crystallinity of the film. That is why the high nitrogen content in the HN2 sample results in the coating exhibiting a pure FCC crystallographic structure. This effect is further supported by the high-entropy effect, which enhances solid solubility among the metal elements and promotes the formation of a single-phase crystallographic structure. Similar observations have been reported for other HEN materials [53,91,92]. The transition to a pure nitride FCC structure occurs via an intermediate FCC nanocrystalline approaching phase, as indicated by the XRD pattern of sample HN1.

The BCC–FCC transition is also supported by mass density measurements performed using the XRR technique. Figure 5b presents the experimental XRR data (scattered dots) and the simulated XRR patterns (continuous lines). Figure 5c shows the evolution of the average mass density deduced from the simulation of the experimental XRR patterns. An almost linear increase in mass density with nitrogen concentration is observed from about 5.49 g/cm^3 (sample H3) to about 6.33 g/cm^3 (sample HN2). This is due to the packing ratio of the FCC structure, which is theoretically about 0.74, being much larger than that of the BCC structure, which is about 0.68. Densification resulting from a BCC to FCC transition has been also observed experimentally in other systems [93,94].

The cross-sectional SEM investigations, presented in Figure 6d–f for samples H3, HN1, and HN2, demonstrate a dense, close-packed columnar structure for the metallic sample, which becomes denser and almost glassy when nitrogen is added (sample HN1), confirming its NC/A structure. As the nitrogen content is further increased (sample HN3), large, well-defined crystalline columnar structures are observed, which is in good agreement with the XRD data. The surface morphology, presented in Figure 6a–c, reveals that samples H3 and HN1 exhibit fine, domed columnar grains, while HN2 shows larger, more developed grains. Correspondingly, the root mean square (RMS) surface roughness is about 0.59 nm for sample H3; it decreases to 0.24 nm for HN1 (indicating a smoother surface due to densification and amorphization), and it increases to 0.93 nm for sample HN2, reflecting the increased crystallinity and the development of larger grains.

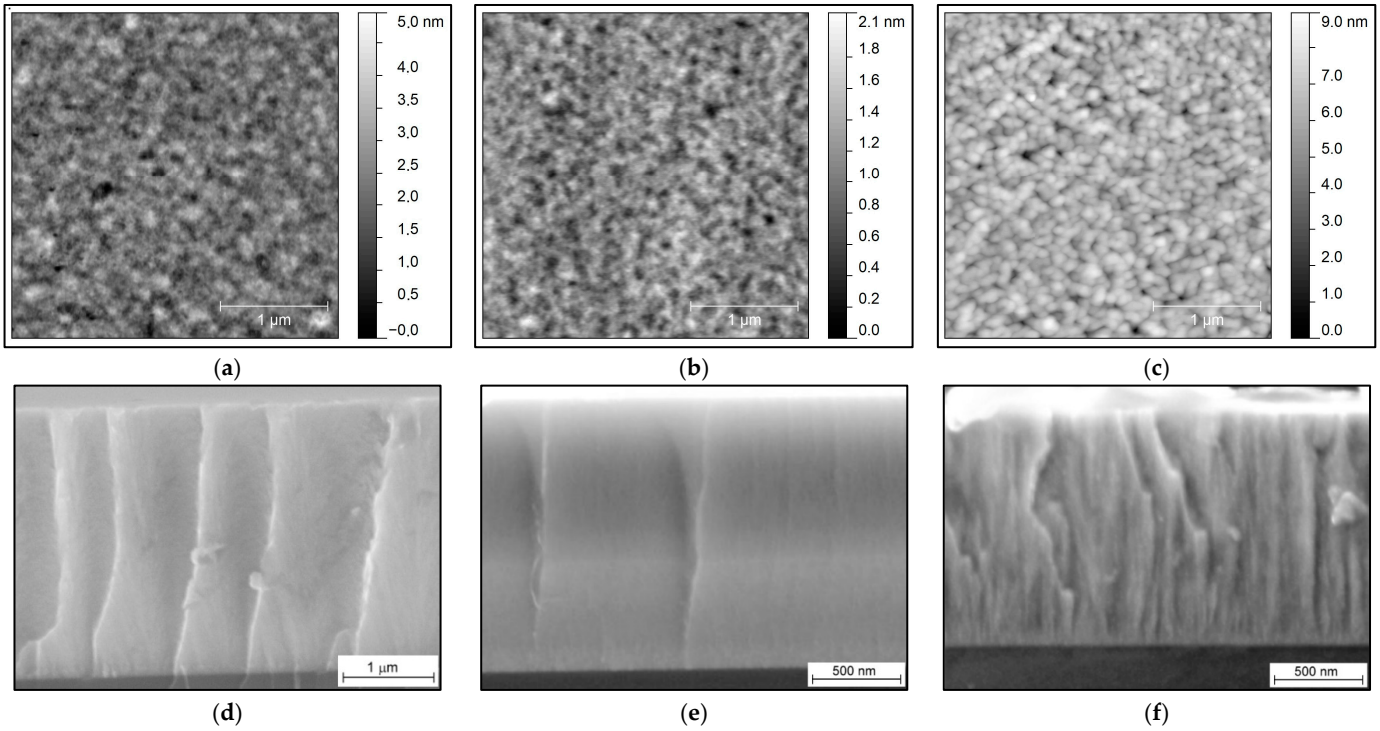

Figure 6. AFM surface images (3 × 3 µm^2) corresponding to (**a**) H3, (**b**) HN1, and (**c**) HN2 samples. Cross-sectional HR-SEM images corresponding to (**d**) H3, (**e**) HN1, and (**f**) HN2 samples.

3.2.2. Mechanical and Tribological Properties of $(TiAl_{0.5}CrNbY)N_y$/C45 ($0 \leq y \leq 0.85$)

Figure 7a presents the evolution of the microhardness and the elastic modulus with increasing nitrogen content. Compared to the metallic sample H3, the HEN coatings exhibit significantly enhanced mechanical properties due to the formation of strong nitride bonds. The hardness of the coatings increases from approximately 6.8 GPa (sample H3) to 14.3 GPa (sample HN1), reaching 21.8 GPa when the nitrogen content is about 45.8 at.% (sample HN2). Similarly, the elastic modulus increases from 87.0 GPa (sample H3) to 127.5 GPa (sample HN1) and further to 171.9 GPa (sample HN2). The high elastic modulus of sample HN2 suggests that the material is more brittle.

The mechanical behavior can be further evaluated through the elasticity index (H/E ratio) and resistance to plastic deformation (H^3/E^2 ratio), both of which are crucial for predicting wear resistance. According to Musil's criteria [95], optimal wear-resistant coatings typically have H < 20 GPa, H/E > 0.1, and H^3/E^2 values between ~0.15 and ~0.3. The calculated H/E ratios for samples H3, HN1, and HN2 are 0.08, 0.11, and 0.13, respectively, while the H^3/E^2 ratios are 0.04, 0.18, and 0.34. Among these, HN1 aligns best with Musil's criteria, indicating a more favorable balance between hardness and resistance to deformation, making it a promising candidate for wear-resistant applications.

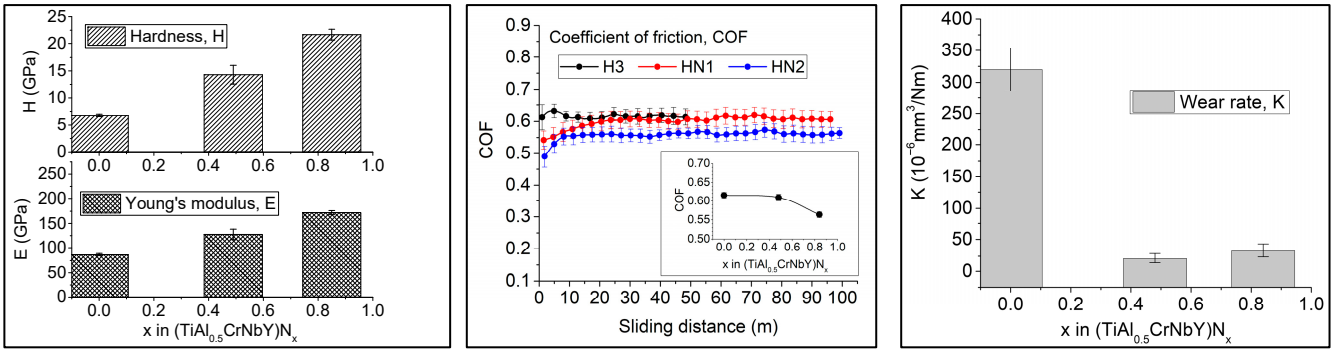

(**a**) (**b**) (**c**)

Figure 7. Mechanical and tribological properties of $(TiAl_{0.5}CrNbY)N_y$/C45 ($0 \leq y \leq 0.85$). (**a**) Hardness (H) and Young's modulus (E). (**b**) Coefficient of friction. (**c**) Wear rate.

The evolution of the friction coefficient (COF) over the sliding distance for samples H3, HN1, and HN2 is shown in Figure 7b. The COF reached a steady state after approximately 20 m of sliding. The mean COF, calculated over the last 20 m of testing, is presented in the inset of Figure 7b, showing a slight decrease with increasing nitrogen concentration, from about 0.61 (sample H3) to approximately 0.57 (sample HN2). The COF of sample HN1 is about 0.60. Although the COF does not change significantly, the wear rate, presented in Figure 7c, shows a substantial decrease between the metallic HEA and the HEN coatings. The wear rate decreases from about $K = 315 \times 10^{-6}$ mm^3/Nm (sample H3) to about 21.2×10^{-6} mm^3/Nm (sample HN1) and increases slightly to about 33.4×10^{-6} mm^3/Nm (sample HN2). Despite the higher microhardness of sample HN2 compared to HN1, the wear rate is slightly higher.

Figure 8 presents the SEM micrographs of the wear track for each sample. The wear track of the metallic sample, H3, is wider, showing characteristics of ductile perforation (adherent material on the wear track and debris particles). In contrast, the HEN specimens exhibited a shallower wear track after 100 m of sliding, with chevron cracks at the border of the wear track and fragmented areas inside of the tracks (as indicated by the arrows). The density of chevron cracks appears to be similar for both HENs, but HN2 shows significantly more fragmentation than HN1.

With a lower elastic modulus, HN1 is slightly more deformable and less brittle than HN2. This gives HN1 a slight advantage in resisting complete fragmentation, even though it displays a similar density of chevron cracks. This suggests that HN1 can absorb more stress before experiencing complete failure, possibly delaying or reducing fragmentation. In contrast, HN2's higher elastic modulus makes it stiffer and more prone to brittle fractures under the same test conditions. This level of stiffness, combined with the high hardness, leads to greater fragmentation because the material cannot absorb stress through plastic deformation, resulting in severe brittle fractures and material disintegration. The key difference in performance between HN1 and HN2 lies in their elastic modulus. HN2, despite having slightly higher hardness, is much stiffer and therefore more brittle, leading to increased fragmentation. For tribological applications, where both wear resistance and toughness are critical, HN1 is more suitable because its lower elastic modulus allows for better stress absorption, thus reducing fragmentation and improving the material's overall durability.

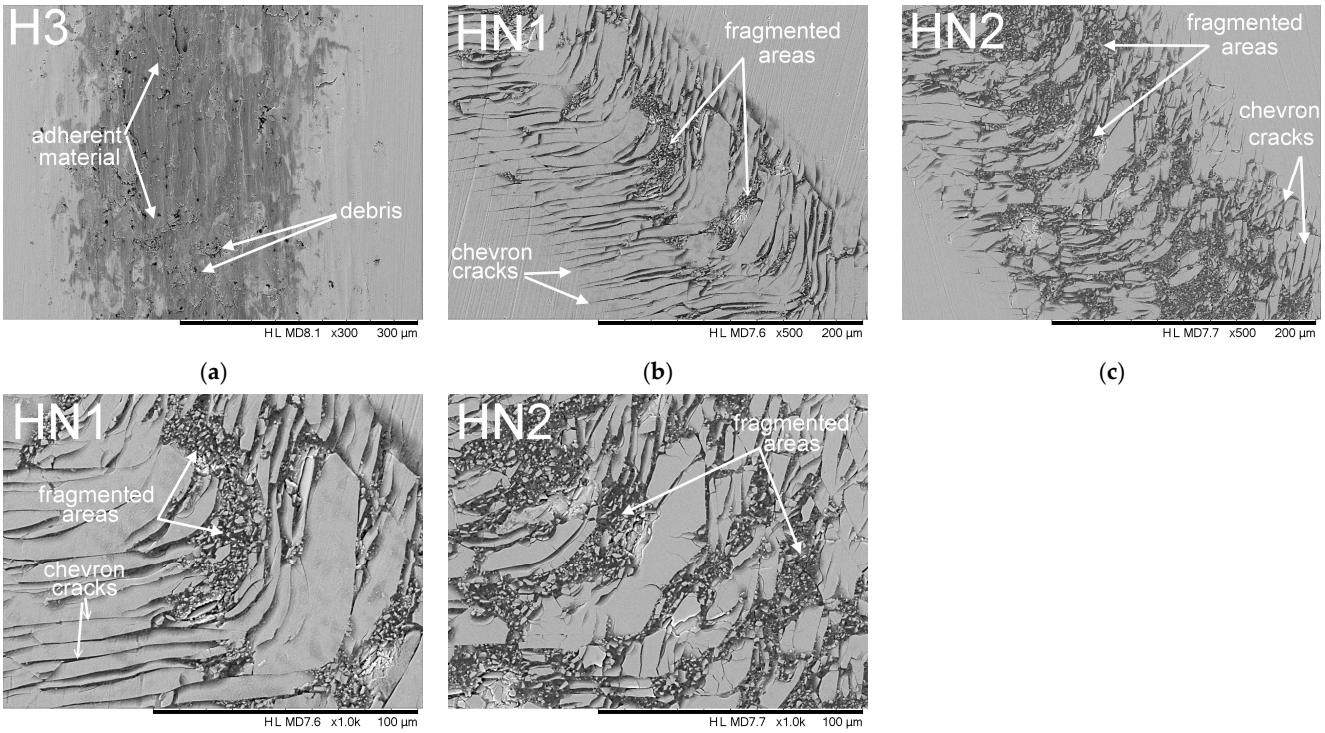

Figure 8. SEM micrographs of wear tracks after tribological test corresponding to samples (**a**) H3 (×300), (**b**) HN1 (×500), and HN2 (×500). Figures (**d**) and (**e**) are magnified views (×1000) of (**b**) and (**c**), respectively.

3.2.3. Electrochemical Evaluation of $(TiAl_{0.5}CrNbY)N_x$ $(0 \leq x = 0.42)$

The impedance data obtained after 12 h immersion in 0.06 M NaCl are presented as Nyquist and Bode amplitudes and phase diagrams (Figure 9), where the resistive and capacitive behaviors of each investigated sample can be assessed. As observed, all of the obtained semicircles (Figure 9a) are characterized by a dominant charge transfer resistance process indicative of the coating's protective nature. Compared with the HEN samples, H3 showed slightly smaller semicircles, suggesting lower overall impedance. Corrosion studies showed that the nitrogen addition (HN1 sample) improved the protective character; however, further increases can be detrimental, and they can trigger the occurrence of a more active corrosion process [96]. This result can be linked to the NC/A nature of the HN1 sample, as demonstrated by XRD and cross-section HR-SEM investigations, whereas HN2 was characterized by a single crystalline FCC nitride phase. At a microscopic level, the formation of a more close-packed columnar structure and its defect-free surface found when a lower N was added (Figure 6b,e) can have a blocking effect, thus acting as a corrosion barrier to the electrolyte ingress [97]. Similar results can be observed in the Bode amplitude graph (Figure 9b), where, in a low-frequency range, the magnitude of impedance ($|Z|$) recorded higher values for HN1, further supporting the previous comments.

In the Bode phase plot (Figure 9c), the more capacitive phase angle of the HN1 sample suggests that the coating is providing a good barrier by preventing the electron/ion flow, and, in this case, the coating acts more like a pure capacitor, potentially offering good corrosion protection.

Although the recorded EIS data did not clearly reveal the presence of two distinct time constants, it is reasonable to interpret the data as a convolution of two phases over the selected immersion time range. Consequently, a two-time constant equivalent circuit, shown in the inset of Figure 9a, was chosen for the fitting procedure, as this provides a more realistic representation of the system. Moreover, because depressed semicircles are displayed in the Nyquist graph, which represent a common feature of solid electrodes and

are often ascribed to surface roughness [98], a constant phase element (CPE) was used in place of a capacitor.

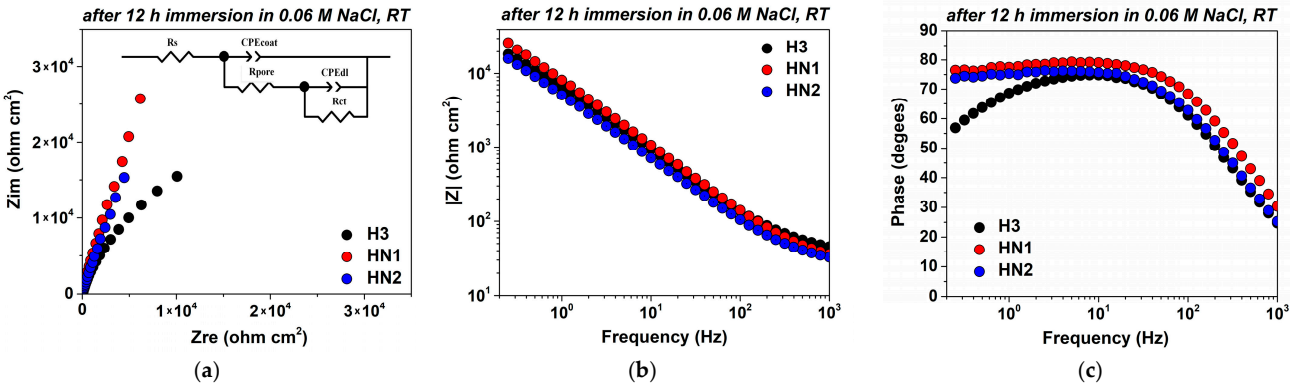

Figure 9. (**a**) Nyquist, (**b**) Bode magnitude, and (**c**) phase diagrams.

The results of the EIS data-fitting procedure are presented in Table 4. As observed, the coatings associated with pseudo-capacitances showed relatively low values, which is typical for dense coatings. Considering the pore resistance, HN1 showed the highest value, indicating better protection against electrolyte ingress through formed pores. The EIS results can be linked to AFM values (Figure 6), where the lowest surface roughness was found when a low quantity of nitrogen was added, closely followed by the metallic sample, which is in direct correlation with the electrochemical behavior. On the other hand, when the added nitrogen reached 0.42%, a greater capacitive contribution can be observed at the interface formed between the substrate and the electrolyte, suggesting in this case a more electroactive area, with the HN2 sample being more prone to corrosion. In agreement, the charge transfer resistance associated with the current flow showed a higher value for HN1, its superior coating protection being attributed to the denser structure.

Table 4. EIS fitted parameters.

Material	R_s (Ω cm^2)	CPE_{coat}		Rpore (Ω cm^2)	CPEdl		R_{ct} (Ω cm^2)
		$Y0_1$ (F cm^{-2} s^{-n})	n_1		$Y0_2$ (F cm^{-2} s^{-n})	n_2	
H3	37	7.69×10^{-6}	0.99	53	2.41×10^{-5}	0.79	51,684
HN1	28	8.47×10^{-6}	0.99	65	1.67×10^{-5}	0.80	646,190
HN2	27	1.06×10^{-5}	0.99	41	3.18×10^{-5}	0.78	511,910

4. Conclusions

This study demonstrated that the microstructure, mechanical properties, tribological performance, and corrosion resistance of $(TiAl_xCrNbY)N_y$ high-entropy coatings synthesized through hybrid HiPIMS/DCMS reactive magnetron sputtering can be tuned by adjusting the aluminum and nitrogen content. Important trends observed include a transition from a crystalline to a nanocrystalline and nearly amorphous (NC/A) structure with increasing aluminum content from 3.0 at. % to 19.8 at. % in $TiAl_xCrNbY$ alloy. The $TiAl_{0.5}CrNbY$ coating (sample H3), with an aluminum content of 11.8%, exhibited the best combination of mechanical and tribological properties, showing moderate hardness (6.8 GPa), a low elastic modulus (87.1 GPa), a reduced wear rate (315×10^{-6} mm^3/Nm), and a high coefficient of friction (0.64).

Further enhancements were observed with the incorporation of nitrogen in the $TiAl_{0.5}CrNbY$ system. XRD and cross-sectional HR-SEM revealed that nitrogen addition led to the formation of a denser, fine-grained structure. As the nitrogen content increased, a transition from a BCC to an FCC structure was observed, accompanied by improvements in

mass density, mechanical properties, and wear resistance. The hardness, the elastic modulus, and the wear rate reached 21.8 GPa, 171.9 GPa, and 33.4 × 10^{-6} mm^3/Nm, respectively, for the $(TiAl_{0.5}CrNbY)N_{0.85}$ coating (HN2 sample) containing 45.8% nitrogen.

Although the HN2 coating exhibited the highest hardness, its higher elastic modulus made it more brittle and prone to fragmentation during wear tests. In contrast, the $(TiAl_{0.5}CrNbY)N_{0.5}$ coating (sample HN1), with 32.9% nitrogen content, demonstrated better toughness and improved wear resistance (21.2 × 10^{-6} mm^3/Nm), along with a high coefficient of friction (0.60). This performance was due to HN1's lower elastic modulus, E = 127.5 GPa, allowing it to absorb more stress.

Electrochemical impedance spectroscopy (EIS) tests showed that the denser and more homogeneous structure of $(TiAl_{0.5}CrNbY)N_{0.5}$ coating acted as an effective barrier against electrolyte ingress, thus preventing corrosion and enhancing durability.

In conclusion, the $(TiAl_{0.5}CrNbY)N_{0.5}$ coating achieved the best overall performance for applications requiring a high coefficient of friction and a low wear rate, such as brake and clutch systems, demonstrating a clear trend towards enhanced durability and stability in frictional environments.

We note that the HiPIMS/DCMS hybrid sputtering process played an important role in this study by enabling the synthesis of $(TiAl_xCrNbY)N_y$ high-entropy coatings with unique microstructural and performance characteristics. Due to presence of HiPIMS processes, the hybrid sputtering technique operates far from thermodynamic equilibrium, and it is able to produce a highly ionized metal plasma, which ensures a more energetic bombardment of the growing film, resulting in better ad-atom mobility, increased adhesion, and densification of the film. The increased ad-atom mobility might also contribute to the development of multiple structural phases. Additionally, the hybrid sputtering process allows for tuning the stoichiometry of the deposited layers via adjusting the frequency of HiPIMS pulses, thus enabling more precise control over the coating's composition and, subsequently, the coating's functional properties, without significant changes in the plasma characteristics.

Author Contributions: Conceptualization, N.C.Z.; methodology, N.C.Z. and M.D.; formal analysis, M.D., A.C.P., A.E.K. and I.P.; investigation, M.D., A.C.P., I.P. and A.E.K.; writing—original draft preparation, N.C.Z. and M.D. All authors have read and agreed to the published version of the manuscript.

Funding: This research was funded by the Core Program within the Romanian National Research Development and Innovation Plan 2022–2027, carried out with the support of MCID, project no. PN 23 05 (id: PN11N-03-01-2023) and by a grant of the Romanian National Authority for Scientific Research and Innovation, CCCDI-UEFISCDI, project number ERANET-M.-TriboHEA, within PNCDI III.

Data Availability Statement: Data are contained within the article.

Acknowledgments: The authors would like to express their gratitude to Aurel Mihai Vlaicu from The National Institute of Materials Physics, Magurele, Romania, for providing the cross-sectional EDS analysis.

Conflicts of Interest: The authors declare no conflicts of interest.

References

1. Cantor, B.; Chang, I.T.H.; Knight, P.; Vincent, A.J.B. Microstructural development in equiatomic multicomponent alloys. *Mater. Sci. Eng. A* **2004**, *375–377*, 213–218. [CrossRef]
2. Yeh, J.-W. Recent progress in high-entropy alloys. *Ann. Chim. Sci. Mater.* **2006**, *31*, 633–648. [CrossRef]
3. Sathiyamoorthi, P.; Kim, H.S. High-entropy alloys with heterogeneous microstructure: Processing and mechanical properties. *Prog. Mater. Sci.* **2022**, *123*, 100709. [CrossRef]
4. Jia, B.; Wan, Q.; Yan, L.; Luo, Y.; Wei, Q.; Niu, C.; Yang, B.; Li, S.; Meng, L. Tribological properties and machine learning prediction of FeCoCrNiAlN high entropy coatings. *Surf. Coat. Technol.* **2024**, *477*, 130341. [CrossRef]
5. Ranganathan, S. Alloyed pleasures: Multimetallic cocktails. *Curr. Sci.* **2003**, *85*, 1404–1406.
6. Yeh, J.-W.; Chen, S.K.; Lin, S.-J.; Gan, J.-Y.; Chin, T.-S.; Shun, T.-T.; Tsau, C.-H.; Chang, S.-Y. Nanostructured high-entropy alloys with multiple principal elements: Novel alloy design concepts and outcomes. *Adv. Eng. Mater.* **2004**, *6*, 299–303. [CrossRef]

7. Zhang, Y.; Zuo, T.T.; Tang, Z.; Gao, M.C.; Dahmen, K.A.; Liaw, P.K.; Lu, Z.P. Microstructures and properties of high-entropy alloys. *Prog. Mater. Sci.* **2014**, *61*, 1–93. [CrossRef]
8. Singh, S.; Wanderka, N.; Murty, B.; Glatzel, U.; Banhart, J. Decomposition in multi-component AlCoCrCuFeNi high-entropy alloy. *Acta Mater.* **2011**, *59*, 182–190. [CrossRef]
9. Tsai, K.-Y.; Tsai, M.-H.; Yeh, J.-W. Sluggish diffusion in Co–Cr–Fe–Mn–Ni high-entropy alloys. *Acta Mater.* **2013**, *61*, 4887–4897. [CrossRef]
10. Tsai, M.-H.; Wang, C.-W.; Tsai, C.-W.; Shen, W.-J.; Yeh, J.-W.; Gan, J.-Y.; Wu, W.-W. Thermal stability and performance of NbSiTaTiZr high-entropy alloy barrier for copper metallization. *J. Electrochem. Soc.* **2011**, *158*, H1161–H1165. [CrossRef]
11. Tsai, M.-H.; Yeh, J.-W.; Gan, J.-Y. Diffusion barrier properties of AlMoNbSiTaTiVZr high-entropy alloy layer between copper and silicon. *Thin Solid Films* **2008**, *516*, 5527–5530. [CrossRef]
12. Ng, C.; Guo, S.; Luan, J.; Shi, S.; Liu, C. Entropy-driven phase stability and slow diffusion kinetics in an $Al_{0.5}$CoCrCuFeNi high entropy alloy. *Intermetallics* **2012**, *31*, 165–172. [CrossRef]
13. Tong, C.-J.; Chen, Y.-L.; Yeh, J.-W.; Lin, S.-J.; Chen, S.-K.; Shun, T.-T.; Tsau, C.-H.; Chang, S.-Y. Microstructure characterization of Al_xCoCrCuFeNi high-entropy alloy system with multiprincipal elements. *Metall. Mater. Trans. A* **2005**, *36*, 881–893. [CrossRef]
14. Shun, T.-T.; Hung, C.-H.; Lee, C.-F. Formation of ordered/disordered nanoparticles in FCC high entropy alloys. *J. Alloys Compd.* **2010**, *493*, 105–109. [CrossRef]
15. Tsai, M.-H.; Yuan, H.; Cheng, G.; Xu, W.; Tsai, K.-Y.; Tsai, C.-W.; Jian, W.W.; Juan, C.-C.; Shen, W.-J.; Chuang, M.-H.; et al. Morphology, structure and composition of precipitates in $Al_{0.3}CoCrCu_{0.5}FeNi$ high-entropy alloy. *Intermetallics* **2013**, *32*, 329–336. [CrossRef]
16. Kumar, J.; Linda, A.; Biswas, K. Lattice distortion in FCC HEAs and its effect on mechanical properties: Critical analysis and way forward. *J. Appl. Phys.* **2023**, *133*, 155102. [CrossRef]
17. Wang, Z.; Fang, Q.; Li, J.; Liu, B.; Liu, Y. Effect of lattice distortion on solid solution strengthening of BCC high-entropy alloys. *J. Mater. Sci. Technol.* **2018**, *34*, 349–354. [CrossRef]
18. Mu, S.; Wimmer, S.; Mankovsky, S.; Ebert, H.; Stocks, G. Influence of local lattice distortions on electrical transport of refractory high entropy alloys. *Scr. Mater.* **2019**, *170*, 189–194. [CrossRef]
19. Adamo, C.G.; Srivastava, A.; Legese, S.S.; Kawamura, Y.; Serbesa, A.T.; Raman, S.P.; Olu, F.E.; Tiwary, C.S.; Singh, A.K.; Chattopadhyay, K. Thermoelectric Transport of a Novel Zr-Based Half-Heusler High-Entropy Alloy. *Energy Technol.* **2024**, *12*, 2301119. [CrossRef]
20. Cheng, B.; Lou, H.; Sarkar, A.; Zeng, Z.; Zhang, F.; Chen, X.; Tan, L.; Prakapenka, V.; Greenberg, E.; Wen, J.; et al. Pressure-induced tuning of lattice distortion in a high-entropy oxide. *Commun. Chem.* **2019**, *2*, 114. [CrossRef]
21. Yeh, J.-W.; Lin, S.-J.; Chin, T.-S.; Gan, J.-Y.; Chen, S.-K.; Shun, T.-T.; Tsau, C.-H.; Chou, S.-Y. Formation of simple crystal structures in Cu-Co-Ni-Cr-Al-Fe-Ti-V alloys with multiprincipal metallic elements. *Met. Mater. Trans. A* **2004**, *35*, 2533–2536. [CrossRef]
22. Cao, B.; Wang, C.; Yang, T.; Liu, C. Cocktail effects in understanding the stability and properties of face-centered-cubic high-entropy alloys at ambient and cryogenic temperatures. *Scr. Mater.* **2020**, *187*, 250–255. [CrossRef]
23. Zhu, S.; Du, W.B.; Wang, X.M.; Han, G.F. High mixing entropy alloys design with high anticorrosion and wear-resistance properties. *Adv. Mater. Res.* **2013**, *815*, 19–24. [CrossRef]
24. Chang, C.-C.; Hsiao, Y.-T.; Chen, Y.-L.; Tsai, C.-Y.; Lee, Y.-J.; Ko, P.-H.; Chang, S.-Y. Lattice distortion or cocktail effect dominates the performance of Tantalum-based high-entropy nitride coatings. *Appl. Surf. Sci.* **2022**, *577*, 151894. [CrossRef]
25. Wang, B.; Yao, Y.; Yu, X.; Wang, C.; Wu, C.; Zou, Z. Understanding the enhanced catalytic activity of high entropy alloys: From theory to experiment. *J. Mater. Chem. A* **2021**, *9*, 19410–19438. [CrossRef]
26. Shi, Z.; Wang, L.; Huang, Y.; Kong, X.Y.; Ye, L. High-entropy catalysts: New opportunities toward excellent catalytic activities. *Mater. Chem. Front.* **2024**, *8*, 179–191. [CrossRef]
27. Liu, X.; Duan, Y.; Yang, X.; Huang, L.; Gao, M.; Wang, T. Enhancement of magnetic properties in $FeCoNiCr_{0.4}Cu_X$ high entropy alloys through the cocktail effect for megahertz electromagnetic wave absorption. *J. Alloys Compd.* **2021**, *872*, 159602. [CrossRef]
28. Kumari, P.; Gupta, A.K.; Mishra, R.K.; Ahmad, M.; Shahi, R.R. A Comprehensive review: Recent progress on magnetic high entropy alloys and oxides. *J. Magn. Magn. Mater.* **2022**, *554*, 169142. [CrossRef]
29. Miracle, D.B. High-entropy alloys: A current evaluation of founding ideas and core effects and exploring "nonlinear alloys". *JOM* **2017**, *69*, 2130–2136. [CrossRef]
30. Chanda, B.; Das, J. An assessment on the stability of the eutectic phases in high entropy alloys. *J. Alloys Compd.* **2019**, *798*, 167–173. [CrossRef]
31. Guo, S.; Hu, Q.; Ng, C.; Liu, C. More than entropy in high-entropy alloys: Forming solid solutions or amorphous phase. *Intermetallics* **2013**, *41*, 96–103. [CrossRef]
32. Zeng, Y.; Man, M.; Bai, K.; Zhang, Y.-W. Revealing high-fidelity phase selection rules for high entropy alloys: A combined CALPHAD and machine learning study. *Mater. Des.* **2021**, *202*, 109532. [CrossRef]
33. Tsai, M.-H.; Tsai, R.-C.; Chang, T.; Huang, W.-F. Intermetallic phases in high-entropy alloys: Statistical analysis of their prevalence and structural inheritance. *Metals* **2019**, *9*, 247. [CrossRef]
34. Tsai, M.-H. Three strategies for the design of advanced high-entropy alloys. *Entropy* **2016**, *18*, 252. [CrossRef]
35. Xing, F.; Ma, J.; Shimizu, K.; Furukawa, S. High-entropy intermetallics on ceria as efficient catalysts for the oxidative dehydrogenation of propane using CO_2. *Nat. Commun.* **2022**, *13*, 5065. [CrossRef]

36. Chen, D.-S.; Chen, M.-K.; Chang, S.-Y. Multiprincipal-element AlCrTaTiZr-nitride nanocomposite film of extremely high thermal stability as diffusion barrier for Cu metallization. *ECS Trans.* **2009**, *19*, 751–762. [CrossRef]
37. Han, R.; Song, H.; Han, L.; An, M. Atomistic insights on the deformation mechanisms of amorphous/crystalline dual-phase high entropy alloys under nanoindentation. *J. Mater. Res. Technol.* **2023**, *25*, 6027–6038. [CrossRef]
38. Ren, H.; Chen, R.; Gao, X.; Liu, T.; Qin, G.; Wu, S.; Guo, J. Insights on mechanical properties of dual-phase high entropy alloys via Y introduction. *J. Alloys Compd.* **2022**, *929*, 167374. [CrossRef]
39. Xu, C.; Geng, N.; Xiang, Q.; Qu, Y.; Yu, B.; Qiu, K. A novel dual phase high entropy casting alloy with high damping capacity. *Mater. Res. Express* **2021**, *8*, 046517. [CrossRef]
40. Malatji, N.; Lengopeng, T.; Pityana, S.; Popoola, A.P.I. Effect of heat treatment on the microstructure, microhardness, and wear characteristics of AlCrFeCuNi high-entropy alloy. *Int. J. Adv. Manuf. Technol.* **2020**, *111*, 2021–2029. [CrossRef]
41. Li, J.; Chen, H.; Feng, H.; Fang, Q.; Liu, Y.; Liu, F.; Wu, H.; Liaw, P.K. Microstructure evolution and deformation mechanism of amorphous/crystalline high-entropy-alloy composites. *J. Mater. Sci. Technol.* **2020**, *54*, 14–19. [CrossRef]
42. Zhang, R.-Z.; Reece, M.J. Review of high entropy ceramics: Design, synthesis, structure and properties. *J. Mater. Chem. A* **2019**, *7*, 22148–22162. [CrossRef]
43. Barbarossa, S.; Orrù, R.; Cao, G.; Balbo, A.; Zanotto, F.; Sani, E. Optical properties of bulk high-entropy diborides for solar energy applications. *J. Alloys Compd.* **2023**, *935*, 167965. [CrossRef]
44. Chen, L.; Zhang, W.; Lu, W.; Wei, B.; Huo, S.; Wang, Y.; Zhou, Y. Low thermal conductivity of dense (TiZrHfVNbTa)C_x high-entropy carbides by tailoring carbon stoichiometry. *J. Adv. Ceram.* **2023**, *12*, 49–58. [CrossRef]
45. Zoita, N.C.; Dinu, M.; Parau, A.C.; López-Ortega, A.; Pana, I.; Grigorescu, C.E.A.; Mondragon, M.; Sobetkii, A.; Almandoz, X.; Rodriguez, J.C.; et al. The characteristics of light (TiCr$Al_{0.5}$NbCu)C_xN_y high-entropy coatings deposited using a HiPIMS/DCMS technique. *Crystals* **2023**, *13*, 1565. [CrossRef]
46. Su, W.; Chen, L.; Zhang, W.; Huo, S.; Wang, Y.; Zhou, Y. Insights into grain boundary segregation and solubility limit of Cr in (TiZrNbTaCr)C. *J. Mater. Sci. Technol.* **2023**, *139*, 1–9. [CrossRef]
47. Chen, T.; Shun, T.; Yeh, J.; Wong, M. Nanostructured nitride films of multi-element high-entropy alloys by reactive DC sputtering. *Surf. Coat. Technol.* **2004**, *188–189*, 193–200. [CrossRef]
48. Pshyk, A.; Vasylenko, A.; Bakhit, B.; Hultman, L.; Schweizer, P.; Edwards, T.; Michler, J.; Greczynski, G. High-entropy transition metal nitride thin films alloyed with Al: Microstructure, phase composition and mechanical properties. *Mater. Des.* **2022**, *219*, 110798. [CrossRef]
49. Huang, Y.-S.; Chen, L.; Lui, H.-W.; Cai, M.-H.; Yeh, J.-W. Microstructure, hardness, resistivity and thermal stability of sputtered oxide films of AlCoCrCu$_{0.5}$NiFe high-entropy alloy. *Mater. Sci. Eng. A* **2007**, *457*, 77–83. [CrossRef]
50. Schweidler, S.; Tang, Y.; Lin, L.; Karkera, G.; Alsawaf, A.; Bernadet, L.; Breitung, B.; Hahn, H.; Fichtner, M.; Tarancón, A.; et al. Synthesis of perovskite-type high-entropy oxides as potential candidates for oxygen evolution. *Front. Energy Res.* **2022**, *10*, 983979. [CrossRef]
51. Gild, J.; Braun, J.; Kaufmann, K.; Marin, E.; Harrington, T.; Hopkins, P.; Vecchio, K.; Luo, J. A high-entropy silicide: ($Mo_{0.2}Nb_{0.2}Ta_{0.2}Ti_{0.2}W_{0.2}$)$Si_2$. *J. Mater.* **2019**, *5*, 337–343. [CrossRef]
52. Kim, S.J.; Yoon, K.N.; Ko, W.-S.; Park, E.S. Entropy-stabilized silicides: Expanding the B20 single-phase region from mono-silicide to high-entropy silicide. *APL Mater.* **2022**, *10*, 121105. [CrossRef]
53. Oses, C.; Toher, C.; Curtarolo, S. High-entropy ceramics. *Nat. Rev. Mater.* **2020**, *5*, 295–309. [CrossRef]
54. Shen, W.J.; Tsai, M.H.; Tsai, K.Y.; Juan, C.C.; Tsai, C.W.; Yeh, J.W.; Chang, Y.S. Superior oxidation resistance of ($Al_{0.34}Cr_{0.22}Nb_{0.11}Si_{0.11}Ti_{0.22}$)$_{50}N_{50}$ high-entropy nitride. *J. Electrochem. Soc.* **2013**, *160*, C531–C535. [CrossRef]
55. Novikov, V.; Stepanov, N.; Zherebtsov, S.; Salishchev, G. Structure and properties of high-entropy nitride coatings. *Metals* **2022**, *12*, 847. [CrossRef]
56. Arshad, M.; Amer, M.; Hayat, Q.; Janik, V.; Zhang, X.; Moradi, M.; Bai, M. High-entropy coatings (HEC) for high-temperature applications: Materials, processing, and properties. *Coatings* **2022**, *12*, 691. [CrossRef]
57. Firstov, S.A.; Gorban', V.F.; Danilenko, N.I.; Karpets, M.V.; Andreev, A.A.; Makarenko, E.S. Thermal stability of superhard nitride coatings from high-entropy multicomponent Ti–V–Zr–Nb–Hf alloy. *Powder Met. Met. Ceram.* **2014**, *52*, 560–566. [CrossRef]
58. Shen, W.-J.; Tsai, M.-H.; Yeh, J.-W. Machining performance of sputter-deposited ($Al_{0.34}Cr_{0.22}Nb_{0.11}Si_{0.11}Ti_{0.22}$)$_{50}N_{50}$ high-entropy nitride coatings. *Coatings* **2015**, *5*, 312–325. [CrossRef]
59. Kirnbauer, A.; Kretschmer, A.; Koller, C.; Wojcik, T.; Paneta, V.; Hans, M.; Schneider, J.; Polcik, P.; Mayrhofer, P. Mechanical properties and thermal stability of reactively sputtered multi-principal-metal Hf-Ta-Ti-V-Zr nitrides. *Surf. Coat. Technol.* **2020**, *389*, 125674. [CrossRef]
60. Lai, C.-H.; Lin, S.-J.; Yeh, J.-W.; Chang, S.-Y. Preparation and characterization of AlCrTaTiZr multi-element nitride coatings. *Surf. Coat. Technol.* **2006**, *201*, 3275–3280. [CrossRef]
61. Liu, S.; Shi, Z.; Xing, X.; Ren, X.; Zhou, Y.; Yang, Q. Effect of Nb additive on wear resistance and tensile properties of the hypereutectic Fe-Cr-C hardfacing alloy. *Mater. Today Commun.* **2020**, *24*, 101232. [CrossRef]
62. Chapala, P.; Acharyya, S.G.; Shariff, S.M.; Naik, G. Novel Ti-Nb alloys with improved wear resistance for biomedical implant application. In Proceedings of the 2016 38th Annual International Conference of the IEEE Engineering in Medicine and Biology Society (EMBC), Orlando, FL, USA, 16–20 August 2016; IEEE: New York, NY, USA, 2016; pp. 4208–4211.

63. Xiong, H.; Ma, Y.; Zhang, H.; Chen, L. Design of Cu–Cr alloys with high strength and high ductility based on first-principles calculations. *Metals* **2022**, *12*, 1406. [CrossRef]
64. Guo, X.; Xiao, Z.; Qiu, W.; Li, Z.; Zhao, Z.; Wang, X.; Jiang, Y. Microstructure and properties of Cu-Cr-Nb alloy with high strength, high electrical conductivity and good softening resistance performance at elevated temperature. *Mater. Sci. Eng. A* **2019**, *749*, 281–290. [CrossRef]
65. Stepanov, N.; Shaysultanov, D.; Chernichenko, R.; Tikhonovsky, M.; Zherebtsov, S. Effect of Al on structure and mechanical properties of Fe-Mn-Cr-Ni-Al non-equiatomic high entropy alloys with high Fe content. *J. Alloys Compd.* **2019**, *770*, 194–203. [CrossRef]
66. Chase, M.W., Jr. NIST-JANAF Themochemical Tables. *J. Phys. Chem. Ref. Data* **1998**, *9*, 1–1951.
67. Kouznetsov, V.; Macák, K.; Schneider, J.M.; Helmersson, U.; Petrov, I. A novel pulsed magnetron sputter technique utilizing very high target power densities. *Surf. Coat. Technol.* **1999**, *122*, 290–293. [CrossRef]
68. Zoita, N.; Dinu, M.; Kiss, A.; Logofatu, C.; Braic, M. A comparative investigation of hetero-epitaxial TiC thin films deposited by magnetron sputtering using either hybrid DCMS/HiPIMS or reactive DCMS process. *Appl. Surf. Sci.* **2021**, *537*, 147903. [CrossRef]
69. Nečas, D.; Klapetek, P. Gwyddion: An open-source software for SPM data analysis. *Open Phys.* **2012**, *10*, 181–188. [CrossRef]
70. *ISO 14577-1:2015*; Metallic Materials—Instrumented Indentation Test for Hardness and Materials Parameters—Part 1: Test Method. International Organization for Standardization: Geneva, Switzerland, 2015.
71. Patterson, A.L. The scherrer formula for X-ray particle size determination. *Phys. Rev. B* **1939**, *56*, 978–982. [CrossRef]
72. Guo, S.; Ng, C.; Lu, J.; Liu, C.T. Effect of valence electron concentration on stability of fcc or bcc phase in high entropy alloys. *J. Appl. Phys.* **2011**, *109*, 103505. [CrossRef]
73. Guo, S. Phase selection rules for cast high entropy alloys: An overview. *Mater. Sci. Technol.* **2015**, *31*, 1223–1230. [CrossRef]
74. Guo, S.; Liu, C.T. Phase stability in high entropy alloys: Formation of solid-solution phase or amorphous phase. *Prog. Nat. Sci. Mater. Int.* **2011**, *21*, 433–446. [CrossRef]
75. Senkov, O.N.; Scott, J.M.; Senkova, S.V.; Miracle, D.B.; Woodward, C.F. Microstructure and room temperature properties of a high-entropy TaNbHfZrTi alloy. *J. Alloys Compd.* **2011**, *509*, 6043–6048. [CrossRef]
76. Zhang, H.; Zhao, Y.; Huang, S.; Zhu, S.; Wang, F.; Li, D. Manufacturing and analysis of high-performance refractory high-entropy alloy via selective laser melting (SLM). *Materials* **2019**, *12*, 720. [CrossRef]
77. Braic, M.; Braic, V.; Balaceanu, M.; Zoita, C.; Vladescu, A.; Grigore, E. Characteristics of (TiAlCrNbY)C films deposited by reactive magnetron sputtering. *Surf. Coat. Technol.* **2010**, *204*, 2010–2014. [CrossRef]
78. Kube, S.A.; Sohn, S.; Uhl, D.; Datye, A.; Mehta, A.; Schroers, J. Phase selection motifs in High Entropy Alloys revealed through combinatorial methods: Large atomic size difference favors BCC over FCC. *Acta Mater.* **2019**, *166*, 677–686. [CrossRef]
79. Wang, Z.; Guo, S.; Liu, C.T. Phase selection in high-entropy alloys: From nonequilibrium to equilibrium. *JOM* **2014**, *66*, 1966–1972. [CrossRef]
80. Tsai, M.-H.; Yeh, J.-W. High-entropy alloys: A critical review. *Mater. Res. Let.* **2014**, *2*, 107–123. [CrossRef]
81. Miracle, D.B.; Senkov, O.N. A critical review of high entropy alloys and related concepts. *Acta Mater.* **2017**, *122*, 448–511. [CrossRef]
82. Yang, X.; Zhang, Y. Prediction of high-entropy stabilized solid-solution in multi-component alloys. *Mater. Chem. Phys.* **2012**, *132*, 233–238. [CrossRef]
83. Takeuchi, A.; Inoue, A. Classification of bulk metallic glasses by atomic size difference, heat of mixing and period of constituent elements and its application to characterization of the main alloying element. *Mater. Trans.* **2005**, *46*, 2817–2829. [CrossRef]
84. Xiao, L.; Zheng, Z.; Guo, S.; Huang, P.; Wang, F. Ultra-strong nanostructured CrMnFeCoNi high entropy alloys. *Mater. Des.* **2020**, *194*, 108895. [CrossRef]
85. Reverte, E.; Keller, C.; Calvo-Dahlborg, M.; Alcalá, G.; Campos, M.; Cornide, J. Effect of Y_2O_3 addition on the microstructure and mechanical properties of an $Al_{1.8}CoCrCu_{0.5}FeNi$ BCC HEA. *J. Alloys Compd.* **2023**, *960*, 170647. [CrossRef]
86. Schiøtz, J.; Di Tolla, F.D.; Jacobsen, K.W. Softening of nanocrystalline metals at very small grain sizes. *Nature* **1998**, *391*, 561–563. [CrossRef]
87. Ranjith, R.; Giridharan, P.K.; Velmurugan, C.; Chinnusamy, C. Formation of lubricated tribo layer, grain boundary precipitates, and white spots on titanium-coated graphite–reinforced hybrid composites. *J. Aust. Ceram. Soc.* **2019**, *55*, 645–655. [CrossRef]
88. Halder, N.C.; Wagner, C.N.J. Separation of particle size and lattice strain in integral breadth measurements. *Acta Crystallogr.* **1966**, *20*, 312–313. [CrossRef]
89. Liang, S.-C.; Tsai, D.-C.; Chang, Z.-C.; Sung, H.-S.; Lin, Y.-C.; Yeh, Y.-J.; Deng, M.-J.; Shieu, F.-S. Structural and mechanical properties of multi-element (TiVCrZrHf)N coatings by reactive magnetron sputtering. *Appl. Surf. Sci.* **2011**, *258*, 399–403. [CrossRef]
90. Wade, K. Metal-metal and metal-carbon bond energy terms for the rhodium carbonyl clusters $Rh_4(CO)_{12}$ and $Rh_6(CO)_{16}$. *Inorg. Nucl. Chem. Lett.* **1978**, *14*, 71–74. [CrossRef]
91. Chen, L.; Li, W.; Liu, P.; Zhang, K.; Ma, F.; Chen, X.; Zhou, H.; Liu, X. Microstructure and mechanical properties of $(AlCrTiZrV)N_x$ high-entropy alloy nitride films by reactive magnetron sputtering. *Vacuum* **2020**, *181*, 109706. [CrossRef]
92. Lewin, E. Multi-component and high-entropy nitride coatings—A promising field in need of a novel approach. *J. Appl. Phys.* **2020**, *127*, 160901. [CrossRef]
93. Magomedov, M.N. Study of the FCC-BCC phase transition in an Au-Fe alloy. *Phys. Solid State* **2022**, *63*, 2135. [CrossRef]

94. Haraguchi, T.; Otsubo, K.; Sakata, O.; Fujiwara, A.; Kitagawa, H. Remarkable lattice shrinkage in highly oriented crystalline three-dimensional metal–organic framework thin films. *Inorg. Chem.* **2015**, *54*, 11593–11595. [CrossRef] [PubMed]
95. Musil, J.; Novák, P.; Čerstvý, R.; Soukup, Z. Tribological and mechanical properties of nanocrystalline-TiC/a-C nanocomposite thin films. *J. Vac. Sci. Technol. A* **2010**, *28*, 244–249. [CrossRef]
96. Lou, B.-S.; Lin, R.-Z.; Li, C.-L.; Lee, J.-W. Fabrication of (TiZrNbSiMo)1-xNx high entropy alloy coatings using a high power impulse magnetron sputtering technique: Effects of nitrogen addition. *Surf. Coat. Technol.* **2024**, *483*, 130772. [CrossRef]
97. Hung, S.-B.; Wang, C.-J.; Chen, Y.-Y.; Lee, J.-W.; Li, C.-L. Thermal and corrosion properties of V-Nb-Mo-Ta-W and V-Nb-Mo-Ta-W-Cr-B high entropy alloy coatings. *Surf. Coat. Technol.* **2019**, *375*, 802–809. [CrossRef]
98. Gourbeyre, Y.; Tribollet, B.; Dagbert, C.; Hyspecka, L. A physical model for anticorrosion behavior of duplex coatings. *J. Electrochem. Soc.* **2006**, *153*, B162–B168. [CrossRef]